Evaluation of the cloud thermodynamic phase in a climate model using CALIPSO-GOCCP

Grégory Cesana, Hélène Chepfer

Evaluation of the cloud thermodynamic phase in a climate model using CALIPSO-GOCCP

Grégory Cesana[1] and Hélène Chepfer[1]

Received 11 June 2012; revised 22 March 2013; accepted 25 March 2013; published 29 July 2013.

[1] Level 1 measurements, including cross-polarized backscatter, from the Cloud-Aerosol Lidar with Orthogonal Polarization lidar, have been used to document the vertical structure of the cloud thermodynamic phase at global scale. We built a cloud phase identification (liquid, ice, or undefined) in the Global Climate Model (GCM)–oriented Cloud-Aerosol Lidar and Infrared Pathfinder Satellite Observation (CALIPSO) Cloud Product (GOCCP) and analyzed the spatial distribution of liquid and ice clouds in five January, February, March (JFM) seasons of global-scale observations (2007–2011). We developed a cloud phase diagnosis in the Cloud Feedback Model Intercomparison Program Observation Simulator Package to evaluate the cloud phase description in the LMDZ5B climate model. The diagnosis in the simulator is fully consistent with the CALIPSO-GOCCP observations to ensure that differences between the observations and the "model + simulator" ensemble outputs can be attributed to model biases. We compared the liquid and ice cloud vertical distributions simulated by the model with and without the simulator to quantify the impact of the simulator. The model does not produce liquid clouds above 3 km and produces ice instead of liquid at low and middle altitudes in polar regions, as well as along the Intertropical Convergence Zone. The model is unable to replicate the observed coexistence of liquid and ice cloud between 0°C and −40°C. Liquid clouds dominate $T > -21$°C in the observations, $T > -12$°C in the model + simulator, and $T > -7.5$°C in the model parameterization. Even if the simulator shifts the model cloud phase parameterization to colder temperature because of the lidar instrument peculiarities, the cloud phase transition remains too warm compared to the observations.

Citation: Cesana, G., and H. Chepfer (2013), Evaluation of the cloud thermodynamic phase in a climate model using CALIPSO-GOCCP, *J. Geophys. Res. Atmos.*, *118*, 7922–7937, doi:10.1002/jgrd.50376.

1. Introduction

[2] Water coexists in three thermodynamic states (gas, liquid, and solid) in the atmosphere. This state impacts directly the Earth's energetic balance: changes in water states are accompanied by a release of latent heat, and the interactions between water and radiation depend on it. As an example, while water vapor mostly contributes to the greenhouse effect that warms the Earth, dense liquid clouds have a strong albedo effect that cools it, and cold semitransparent ice clouds produce both albedo and greenhouse effects [e.g., *Kiehl and Trenberth*, 1997]. For the above reasons, characterizing the energy exchanges, which take place in the atmosphere, necessitates knowing precisely not only the amount and spatiotemporal distribution of clouds but also their partition between liquid and ice water.

[3] In theory, the local amount of liquid and ice water in the atmosphere is predictable from the temperature and the partial water vapor pressure as described by the Clausius-Clapeyron equation: when the water vapor pressure is sufficient, liquid water particles will form at temperatures above 0°C, whereas ice will form below −40°C. Between 0°C and −40°C, either ice or liquid particles can form, depending on the water vapor available and (to a smaller extent) on the amount and type of condensation and ice nuclei available. However, environmental conditions (temperature, water vapor, and nuclei) are not known at global scale with enough precision and spatiotemporal resolution for the theory to predict the cloud thermodynamic phase all over the globe.

[4] As a consequence, the description of liquid and ice clouds in climate models is poorly constrained due to the lack of adequate information either on the environmental conditions that pilot the water phase or on the liquid and ice water distributions in the atmosphere. This lack of knowledge has led to different (and unverified) descriptions of cloud thermodynamic phase from one model to another, which contributes to cloud climate feedback uncertainties [e.g., *Yokohata et al.*, 2005], and may limit the ability of the climate model to reproduce observed net radiative fluxes in specific regions such as the Arctic [e.g., *Cesana et al.*, 2012].

[5] Most of our knowledge of cloud thermodynamic phase at global scale is derived indirectly from brightness

[1]Laboratoire de Météorologie Dynamique, Institut Pierre-Simon Laplace, Université Pierre et Marie Curie, Paris, France.

Corresponding author: G. Cesana, Laboratoire de Météorologie Dynamique, Institut Pierre-Simon Laplace, Ecole Polytechnique, Rt. de Saclay, FR-91128 Palaiseau CEDEX, France. (gregory.cesana@lmd.polytechnique.fr)

2169-897X/13/10.1002/jgrd.50376

temperature measurements collected by satellites, such as Moderate Resolution Imaging Spectroradiometer (MODIS) [*Barnes et al*., 1998; *Platnick et al*., 2003] and International Satellite Cloud Climatology Project (ISCCP) [*Rossow and Schiffer*, 1999]. The radiometers Polarization and Directionality of the Earth's Reflectances (POLDER) [*Deschamps et al*., 1994] or Polarization and Anisotropy of Reflectances for Atmospheric Sciences Coupled with Observations from a Lidar use an original technique: they measure the state of polarization of the scattered solar light, which directly gives the sphericity (liquid droplet) or nonsphericity (ice crystals) of cloud particles [*Goloub et al*., 2000]. POLDER observations have been used to evaluate the description of the thermodynamic phase in LMDZ [*Doutriaux-Boucher and Quaas*, 2004]. This cloud phase measurement has the advantage of being independent of the temperature but gives only vertically integrated information on the cloud phase. Since June 2006, vertical profiles of depolarization are directly measured by the Cloud-Aerosol Lidar with Orthogonal Polarization [CALIOP on board Cloud-Aerosol Lidar and Infrared Pathfinder Satellite Observation (CALIPSO)] lidar [*Winker et al*., 2009] every one-third kilometer with a laser beam diameter of 70 m and a vertical resolution of 30–60 m. These measurements give information on the sphericity of the cloud particles. As a consequence, the observations contain direct information on the vertical distribution of the thermodynamic water phase of clouds.

[6] The definition of clouds or cloud types is not unique. It differs among observations (e.g., clouds detected by a lidar may not be detected by a radar or by passive remote sensing), among climate models (e.g., conversion from condensed water to cloud cover is not direct), and between models and observations (e.g., models predict clouds at each atmospheric level where condensation occurs, while observations may not detect clouds overlapped by thick upper level clouds). A comparison between modeled and observed clouds thus requires a consistent definition of clouds, which takes into account the effects of viewing geometry, sensors' sensitivity, and vertical overlap of cloud layers. For this purpose, clouds simulated by climate models are often compared to observations through a model-to-satellite approach: model outputs are used to diagnose some quantities that would be observed from space if satellites were flying above an atmosphere similar to that predicted by the model [e.g., *Klein and Jakob*, 1999; *Webb et al*., 2001; *Zhang et al*., 2005; *Bodas-Salcedo et al*., 2008; *Chepfer et al*., 2008; *Marchand et al*., 2009; *Cesana and Chepfer*, 2012].

[7] Within the framework of the Cloud Feedback Model Intercomparison Project (CFMIP, http://www.cfmip.net), which is now coordinated as part of the Coupled Model Intercomparison Project Phase 5 (CMIP5) [*Taylor et al*., 2012], a package named COSP ("CFMIP Observation Simulator Package") [*Bodas-Salcedo et al*., 2011] has been developed to evaluate in a consistent way the cloud cover predicted by climate models with that derived from different satellite observations. This software simulates observations that would be collected by satellites flying over the atmosphere predicted by a model. It is used within CMIP5 and CFMIP2 experiments to evaluate the cloud cover and vertical distribution in climate models by comparing actual satellite observations with synthetic ones. COSP contains a subgridding module called Subgrid Cloud Overlap Profile Sampler [*Klein and Jakob*, 1999]. It generates stochastically 50 subgrid columns from each model gridbox and includes modules to simulate several satellite instruments: CALIPSO [*Chepfer et al*., 2008], CloudSat [*Marchand et al*., 2009], ISCCP [*Klein and Jakob*, 1999; *Webb et al*., 2001], MODIS [*Pincus et al*., 2012], and Multiple Imaging Spectroradiometer [*Marchand and Ackerman*, 2010].

[8] This current study has a dual purpose. The first is to document and better understand the partition of liquid and ice water within clouds at global scale by using a new cloud phase climatology called Global Climate Model (GCM)–oriented CALIPSO Cloud Product (CALIPSO-GOCCP). The second is to propose a methodology to evaluate the description of liquid and ice clouds in climate models. For these purposes, we analyze polarized lidar profiles (Level 1, version 3) observed from CALIOP (section 2) and discriminate liquid and ice clouds. By using the output from the LMDZ5B climate model, we simulate the polarized profiles that would be observed by a lidar flying over the modeled atmosphere (section 3). Then, we define a diagnosis to discriminate the cloud phase (ice/liquid/undefined) at each altitude level within a lidar profile. In section 4, we apply this diagnosis identically to the observed and simulated lidar profiles and build global maps of cloud phase (observed and simulated) by accumulating several months of data. We then compare the cloud phase distributions deduced from the observations with the ones simulated by the ensemble "model + lidar simulator," and we evaluate the cloud thermodynamic phase in the atmospheric component of the Institut Pierre-Simon Laplace climate model.

2. Observation of Cloud Thermodynamic Phase With the CALIOP Lidar on Board CALIPSO

2.1. Physical Basis

[9] Previous studies [*Hu*, 2007; *Hu et al*., 2009, 2010; *Yoshida et al*., 2010; *Cheng et al*., 2012] retrieved the cloud thermodynamic phase using a relationship between the depolarization ratio and the attenuated backscatter profiles measured from CALIOP. In contrast to the studies mentioned above, our diagnosis uses CALIPSO version 3 measurements of attenuated total backscatter (ATB) and cross-polarized ATB ($ATB_{\perp}$) at a fixed vertical resolution of 480 m to discriminate liquid and ice clouds.

[10] First, the cloud is detected using the CALIPSO-GOCCP algorithm [*Chepfer et al*., 2010] designed to evaluate cloud distribution in climate models. It uses lidar profiles collected every 330 m along the satellite flight track at a fixed vertical resolution of 480 m. Cloud detection is applied to each pixel of each lidar profile: the pixel is flagged as cloudy if the value of the scattering ratio ($SR = ATB/ATB_{mol}$) is higher than 5. ATB is the attenuated backscatter, and ATB_{mol} is the attenuated backscatter in clear sky (no particles, only molecules). Figure 1a shows an example of cloud detection along a single CALIOP orbit.

[11] Second, the cloud phase discrimination uses the possible change in the state of polarization of the laser light backscattered (scattering angle $\Theta = \pi$) by the particles

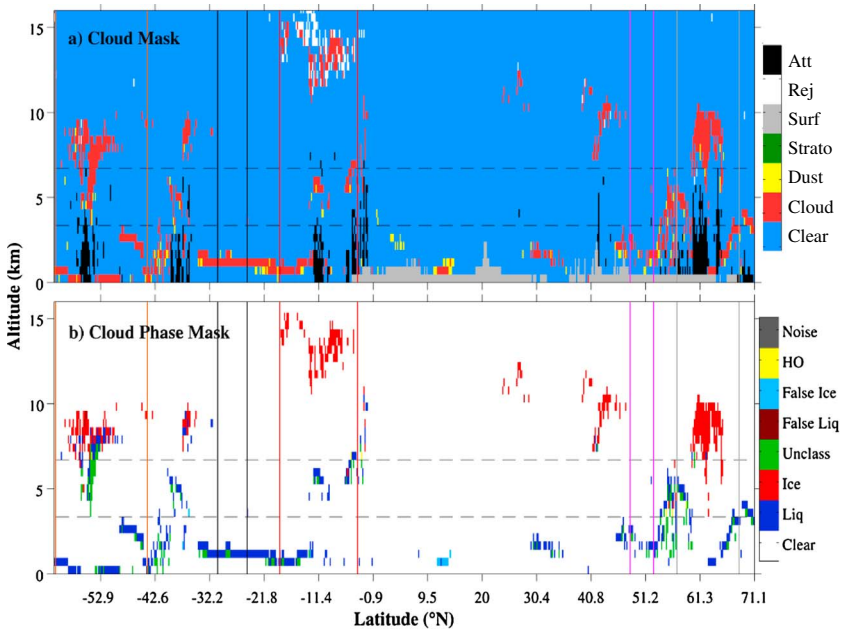

Figure 1. CALIPSO orbit, 1 January 2007 during nighttime (latitude between 72°13′ and −58°93′; longitude between 173°85′ and −4°86′). (a) Cloud mask CALIPSO-GOCCP. (b) Cloud phase mask CALIPSO-GOCCP. "Noise" stands for nonphysical value (depolarization ratio higher than 1), "HO" for horizontally oriented particles, "False Liq" for cloudy pixels classified as liquid (respectively ice) while temperature is lower than −42°C (respectively higher than 0°C), and "Unclass" for cloud located below a cloudy pixel with SR > 30. The temperature is taken from GMAO data (Global Modeling and Assimilation Office) [*Bey et al.*, 2001], which is part of CALIPSO Level 1 ancillary data. For each CALIOP Level 1 profile, we interpolate the GMAO temperature over the 480 m vertical levels of CALIPSO-GOCCP and use it as the cloudy pixel temperature.

composing the cloud. The incident laser light is initially linearly polarized, and after backscattering by the cloud particles, the lidar telescope measures (1) the backscattered attenuated signal collected in the cross-polarized direction ($ATB_\perp$) relative to the incident laser light and (2) the total backscatter attenuated signal ($ATB = ATB_\perp + ATB_{/\!/}$). If the effects of multiple scattering are neglected, the spherical particles (liquid droplets) do not change the state of polarization of the backscatter light, for a scattering angle of 180° exactly leading to $ATB_\perp = 0$ [i.e., *Van de Hulst*, 1957; *Mishchenko and Travis*, 1997], whereas backscattering by nonspherical particles (ice crystals) changes the state of polarization, leading to large values of $ATB_\perp$ at 180°. Multiple scattering effects modify this simple view [*Platt*, 1981], by increasing the $ATB_\perp$ for liquid clouds, because some scattering occurs at scattering angles slightly different from 180° within azimuthal planes different from the incident one, and produce $ATB_\perp$ larger than zero [*Pal and Carswell*, 1985].

2.2. Case Study

[12] Figure 2 shows 2-D histograms of ATB and $ATB_\perp$, called "phase diagrams," obtained for different cloud types defined by their height and temperature. The coldest clouds appear in the tropics (−40°C to −75°C, $z > 8$ km, between red vertical lines in Figure 1a) and polar regions (−40°C to −60°C, not shown). They exhibit similar phase diagrams typical of ice clouds (Figure 2a), which is consistent with the fact that liquid is unlikely at temperatures below −40°C.

[13] Warmer (−10°C to −50°C, $z > 8$ km, between orange vertical lines in Figure 1a) middle-latitude clouds can contain both liquid and ice because they are warmer than the temperature below which homogeneous ice nucleation occurs (about −40°C). As a consequence, the phase diagram for these clouds (Figure 2b) is slightly different from the previous one: a second branch is visible, along near-zero $ATB_\perp$, consistent with the presence of liquid (section 2.1).

[14] Tropical and middle-latitude warm clouds ($z < 3$ km) without any clouds above (between magenta vertical lines in Figure 1a) show a phase diagram typical of liquid water (Figure 2c): $ATB_\perp$ increases slightly with ATB because of multiple scattering [*Sassen and Petrilla*, 1986]. Despite this effect, $ATB_\perp$ remains significantly lower than in ice clouds most of the time. The overall pattern can be clearly discriminated from an ice cloud signature (Figures 2a and 2b), except for $ATB < 0.02\ km^{-1}\ sr^{-1}$.

[15] When we consider more complex scenes, e.g., a low-level cloud with a higher one above or an optically thick stratocumulus (between vertical black lines in Figure 1a), the phase diagrams (Figure 2e) become more complex due to the decreased signal-to-noise ratio. The attenuation of the top cloudy layer within the stratocumulus, as well as the numerous photon reflections inside the cloud, introduce additional noise into the lidar signal particularly in

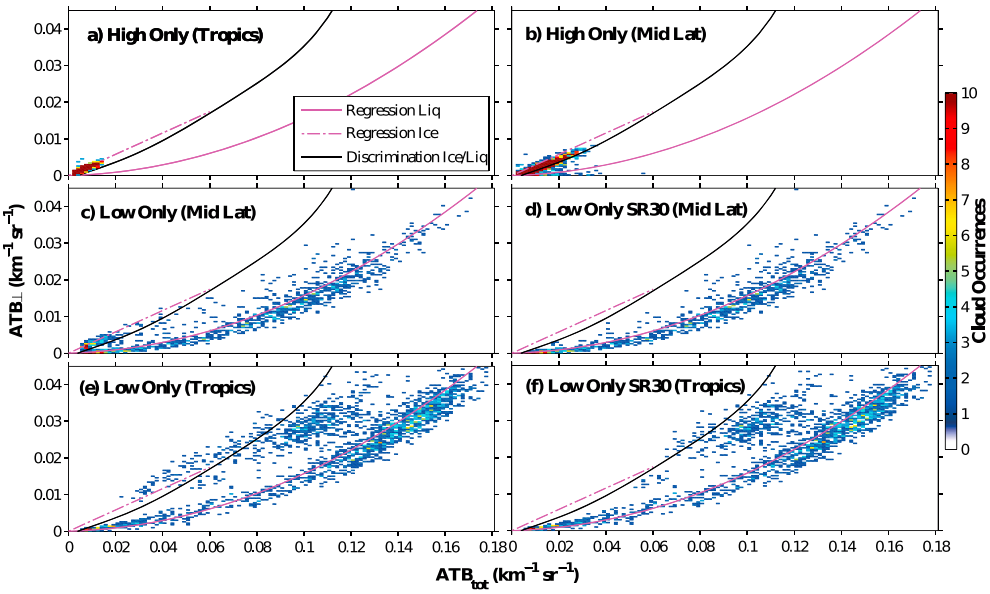

Figure 2. Phase diagrams for different pieces of the orbit. Number of cloudy pixels as a function of the perpendicular attenuated total backscatter (ATB⊥ in the *y* axis) and the attenuated total backscatter (ATB in the *x* axis) observed by CALIPSO at a vertical resolution of $\Delta z = 480$ m. (a) High-altitude ($z > 8$ km) tropical clouds located between the red lines in Figure 1a. (b) High-altitude ($z > 8$ km) middle-latitude clouds located between the orange lines in Figure 1a. (c) Low-altitude ($z < 3$ km) middle-latitude clouds with no high clouds above located between the magenta lines in Figure 1a. (d) Same as Figure 2c but excluding clouds located below another cloud with SR > 30. (e) Low-altitude ($z < 3$ km) stratocumulus clouds located between the black lines in Figure 1a. (f) Same as Figure 2e but excluding clouds located below another cloud with SR > 30. The solid magenta line (respectively dash-dotted magenta) shows the relationship between ATB and ATB⊥ for low cloud pixels only (respectively high clouds). The "phase discrimination line" (black line) is the threshold used to distinguish ice clouds (above the line) from liquid clouds.

the cross-polarized profile. It artificially increases ATB⊥. To avoid false phase detection produced by this additional noise, we exclude the cloudy pixels located at lower altitudes than a cloudy pixel with SR > 30 (Figures 2d and 2f). Comparing Figure 2c with Figure 2d, and Figure 2e with Figure 2f, indicates that most of the cloudy pixels that were behaving like ice in Figures 2c and 2e have been removed.

[16] This case study shows that the phase diagrams may be used to distinguish the water phase. Ice clouds generally have ATB lower than 0.1 km^{-1} sr^{-1} and are located along a straight line (magenta dashed-dotted line in Figure 2). Liquid clouds can have a high value of ATB and are located along a parabolic curve (solid magenta line in Figure 2). As the lidar beam penetrates a dense liquid cloud, the values of ATB as well as ATB⊥ increase due to multiple scattering [*Hu et al.*, 2001], which explains the parabolic shape of the solid magenta line. Moreover, water clouds can produce larger values of ATB than ice clouds because of multiple scattering, larger cloud optical depths, or very small particle radii.

2.3. Statistics Over 3 Months

2.3.1. Cloud Phase Determination

[17] Figure 3 shows the phase diagram obtained when accumulating 3 months (JFM 2010) of CALIPSO-GOCCP observations over the globe. Figure 3a contains all cloudy pixels regardless of their temperature. Figure 3b is for warm ($T > 0°C$ and $z < 3$ km) clouds that can confidently be considered as liquid. Figure 3c is the phase diagram for cold ($T < -40°C$ and $z > 8$ km) clouds only, which can confidently be considered as ice. These statistical diagrams (Figures 3b and 3c) are consistent with the typical behavior observed in the previous case study (Figure 2): cold clouds (Figure 3c) remain along the "ice" parameterization (magenta dashed-dotted line), i.e.,

$$\mathrm{ATB}_{\perp} = 0.29 \cdot \mathrm{ATB} \quad (1)$$

and the warm clouds remain along the "liquid water" parameterization (parabolic magenta curve), i.e.,

$$\mathrm{ATB}_{\perp} = 1.39 \cdot \mathrm{ATB}^2 + 1.76\,10^{-2} \cdot \mathrm{ATB} \quad (2)$$

[18] This suggests that ice and liquid clouds can be distinguished as a function of their ATB and ATB⊥ using a discrimination line. The phase discrimination line (i.e., the black curve in Figures 2 and 3) has been built from the phase diagram (Figure 4a) of the ice fraction with

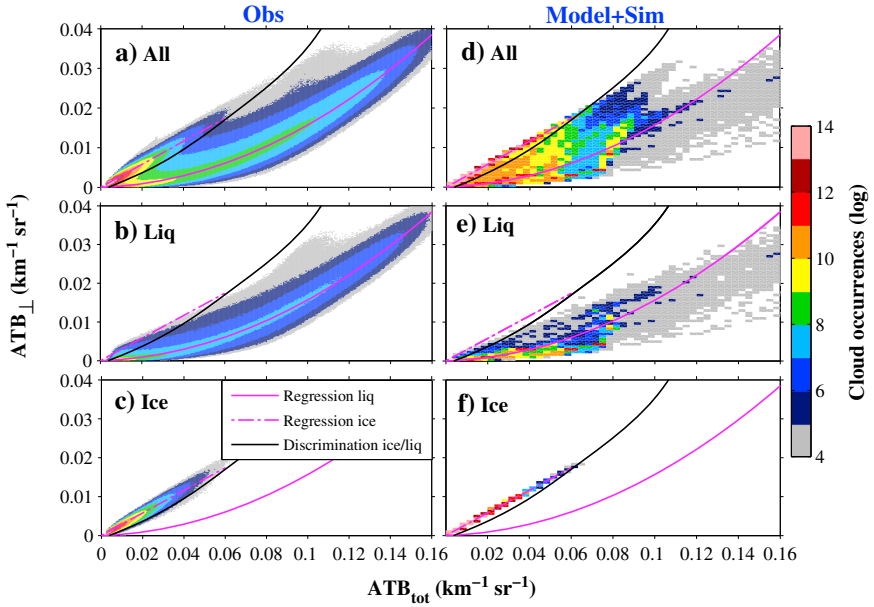

Figure 3. Global phase diagrams. Number of cloudy pixels (log) as a function of the perpendicular attenuated total backscatter (ATB⊥ in the y axis) and the attenuated total backscatter (ATB in the x axis) for JFM 2010 at a vertical resolution of $\Delta z = 480$ m, (left column) as observed by CALIPSO-GOCCP and (right column) as simulated at the subgrid scale by the "LMDZ GCM + COSP lidar simulator." All cloudy pixels regardless of their temperature in (a) observations and (d) simulations. High cold cloudy pixels only ($z > 8$ km and $T < -40°$C) in (b) observations and (e) simulations. Low warm cloudy pixels only ($z < 3$ km and $T > 0°$C) without cloud above in (c) observations and (f) simulations. The solid magenta line (respectively dash-dotted magenta) shows the relationship between ATB and ATB⊥ for low cloud pixels only (respectively high clouds). The "phase discrimination line" (black line) is the threshold used to distinguish ice clouds (above the line) from liquid clouds (below the line).

respect to the total condensate, including only the warm ($T > 0°$C and $z < 3$ km) and cold ($T < -40°$C and $z > 8$ km) cloudy pixels, excluding clouds with temperatures ranging between $-40°$C and $0°$C. The warm (respectively cold) clouds can unambiguously be considered as liquid (respectively ice) and do not content mixed phase. The phase discrimination line is defined as the isoline 50% in Figure 4a: the ice fraction is equal to the liquid fraction. The phase discrimination line fits the following equation:

$$\mathrm{ATB}_{\perp} = 9.032\ 10^{-3}\cdot\mathrm{ATB}^5 + 2.136\ 10^{-3}\cdot\mathrm{ATB}^4 + 173.396\cdot\mathrm{ATB}^3 - 3.951\cdot\mathrm{ATB}^2 + 0.256\cdot\mathrm{ATB} - 9.478\ 10^{-4} \quad (3)$$

[19] The gray (respectively pink) boxes are the ones where warm clouds ($T > 0°$C; respectively cold clouds, $T < -40°$C) represent 100% of the points. The ambiguous region (between 10% and 90% ice fractions in Figure 4a) is relatively thin (blue to red color in Figure 4a) and contains 1.2% of the cloudy pixels. The sensitivity of the results to the position of the phase discrimination line will be discussed in section 4, considering the curve located along the 10% or 90% isolines.

[20] In the rest of the paper, we used the phase diagram to classify each cloudy pixel in each profile as "ice," "liquid," or "undefined" water phase. Cloudy pixels above the phase discrimination line are classified as "ice" and those below as "liquid." The "undefined" class (10.3% of cloudy pixels) contains the ambiguous cloudy pixels: (1) below another cloud with SR > 30 (as discussed in the previous section), (2) with a nonphysical value of depolarization (higher than 1 or ATB// <0 and/or ATB ⊥ <0), and (3) containing typical signatures of horizontally oriented particles (high ATB and ATB⊥ close to 0) [e.g., *Noel and Chepfer*, 2010].

[21] Moreover, cloudy pixels colder than $-42°$C (respectively warmer than $0°$C) but identified as liquid (respectively ice) using the phase diagram are classified as ice (respectively liquid). It represents 0.14% (respectively 0.62%) of all the cloudy pixels, which indicates that the phase discrimination is independent of the temperature in more than 99% of the cases. Figure 1b shows the cloud phase mask obtained when applying this algorithm to the orbit presented in Figure 1a.

2.3.2. Sensitivity of the Phase Diagram to the Vertical Resolution of the Lidar Profiles

[22] For a given vertical resolution, an optically thicker cloud contains more particles, and therefore, the probability for the photon to be scattered before coming back in the lidar telescope [*Pal and Carswell*, 1985] is larger. This is the multiple scattering effect. From this statement, the pattern of the phase diagram is expected to vary as a

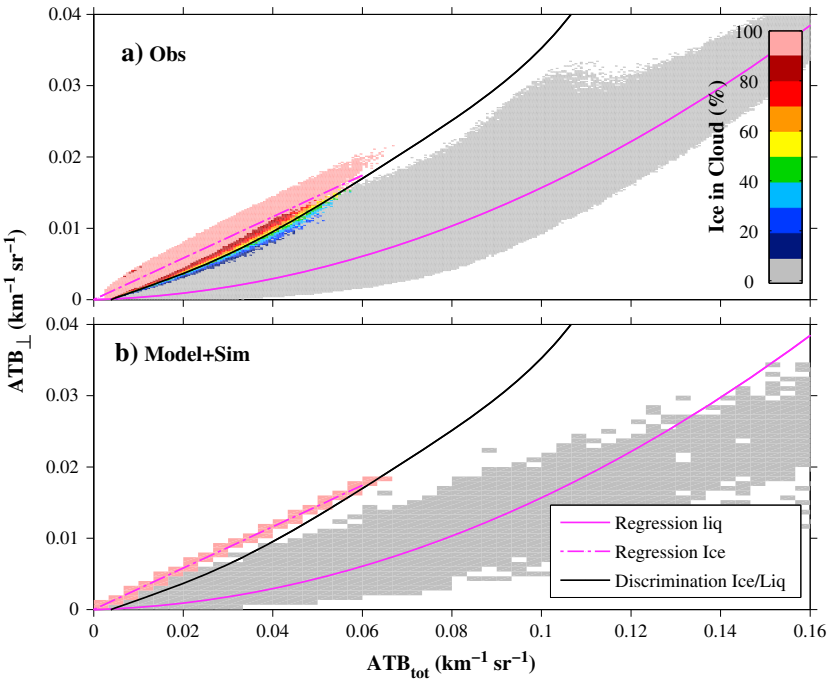

Figure 4. Phase diagrams. Ice fraction with respect to the total condensate as a function of the perpendicular attenuated total backscatter (ATB⊥ in the *y* axis) and the attenuated total backscatter (ATB in the *x* axis) for JFM 2010, at a vertical resolution of $\Delta z = 480$ m, (a) as observed by CALIPSO-GOCCP and (b) as simulated by the "LMDZ GCM + COSP lidar simulator." The solid magenta (respectively dash-dotted magenta) curves show the relationship between ATB and ATB⊥ for warm ($T > 0°C$) clouds only (respectively cold clouds, $T < -40°C$). The phase discrimination line (black line) is the 50% isoline that will be used to distinguish ice clouds (above the line) from liquid clouds (below the line).

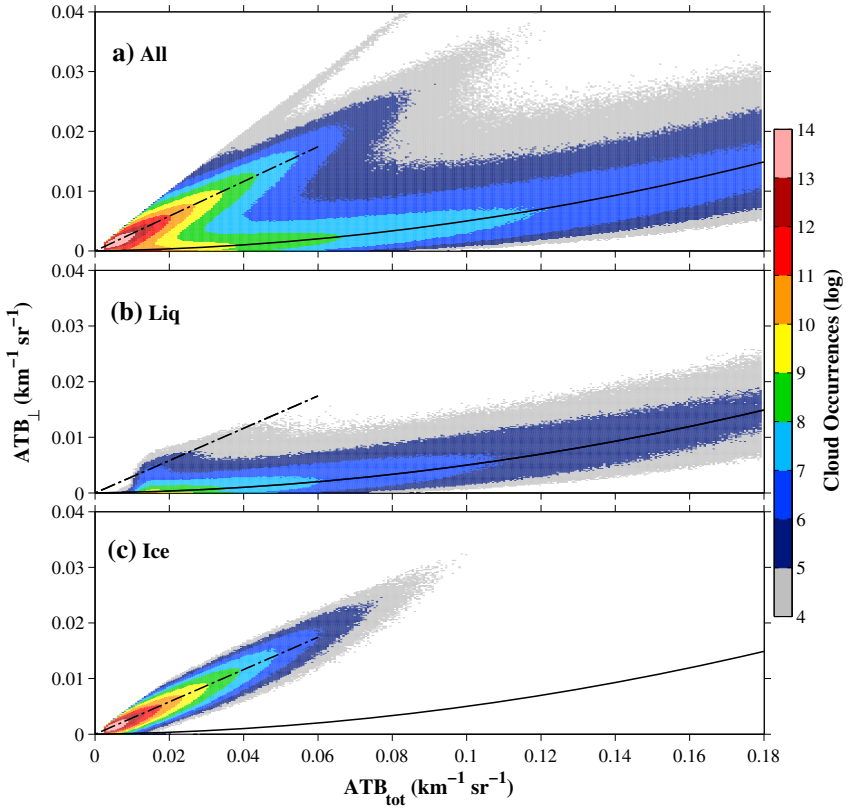

Figure 5. Global phase diagrams. Same as Figures 3a–3c but for $\Delta z = 120$ m.

Table 1. Sensitivity of the Liquid, Ice, Undefined Phase, and All Cloud Cover (JFM) as Simulated by the "LMDZ GCM + COSP/Lidar Simulator" for Different Multiple Scattering Coefficients (η)

	Ice Clouds			Liquid Clouds		
	$\eta = 0.7$	$\eta = 0.5$	$\eta = 0.3$	$\eta = 0.7$	$\eta = 0.5$	$\eta = 0.3$
High	20	19.9	19.6	0	0	0
Middle	10.6	10.4	9.7	1	1.1	1.4
Low	8.1	7.7	7.6	16.9	16.4	15.8
	Undefined Phase Clouds			**All**		
	$\eta = 0.7$	$\eta = 0.5$	$\eta = 0.3$	$\eta = 0.7$	$\eta = 0.5$	$\eta = 0.3$
High	9.4	11.1	13.6	34.4	35.2	37
Middle	4.7	5.65	7.5	16.4	17.2	18.6
Low	0.4	0.5	0.8	20.4	20.4	20.5

function of the vertical resolution of ATB⊥ and ATB. Figure 5 shows the same diagram as in Figures 3a–3c but built with a higher vertical resolution (120 m instead of 480 m). Cold ice clouds show slightly lower values of ATB at 480 m resolution (Figure 3c) than at 120 m resolution (Figure 5c) but show similar pattern regardless of the resolution. This result was expected because multiple scattering has a small impact on ice particles and does not change the relationship between ATB and ATB⊥. On the contrary, for liquid clouds, a lower depolarization was expected. As the lidar beam penetrates less deep in the cloud, the possibility for the photon to encounter another particle and be scattered is lower. This statement is illustrated in Figure 5b: for 120 m heighted clouds, the value of ATB⊥ is lower than for 480 m heighted clouds for a given value of ATB. The impact of the multiple scattering effect on the cloud geometrical thickness has to be taken into account in the parameterization used in the simulator to predict ATB⊥. GCM could have many different vertical resolutions and sometimes thinner than 480 m. That is why the thinnest resolution of CALIPSO-GOCCP has been used to establish the parameterization of ice/liquid ATB⊥ in the lidar simulator (section 3.1).

3. Simulation of the Lidar Polarized Profile From Climate Model Outputs

[23] The lidar module (or "simulator") [*Chepfer et al.*, 2008] currently included in COSP [*Bodas-Salcedo et al.*, 2011] computes CALIPSO-like profiles of ATB and SR from GCM subgridded outputs. In order to evaluate the cloud thermodynamic phase description in climate models, we developed a new cloud phase diagnosis in the lidar simulator, which consists of (1) computing ATB and ATB⊥ that would be observed by CALIPSO above the modeled atmosphere at the subgrid scale; (2) discriminating liquid, ice, or undefined cloudy pixel of the subgrid profile; and (3) building statistical cloud phase diagnosis at global scale.

3.1. Simulations of ATB and ATB⊥ at 532 nm

[24] The standard version of the lidar simulator uses the pressure, temperature, particle size and type, liquid and ice mixing ratios, and cloud fraction produced by the model in each subgrid at each level of altitude to compute the ATB and ATB_{mol} profiles. The ATB and ATB_{mol} profiles are computed using the lidar equation

$$\begin{aligned} ATB(z) = &\left(\beta_{//,liq(z)} + \beta_{\perp,liq(z)} + \beta_{//,ice(z)} \right. \\ &+\beta_{\perp,ice(z)} + \beta_{//,mol(z)} \\ &\left. +\beta_{\perp,mol(z)}\right) \\ &\cdot \exp\left[-2\int_{Z}^{TOA}\left(\eta\left(\alpha_{ice(z)} + \alpha_{liq(z)}\right) + \alpha_{mol(z)}\right)dz\right] \end{aligned} \quad (4)$$

$$ATB_{mol(z)} = \beta_{mol(z)} + \exp\left(\int_{Z}^{TOA}\alpha_{mol(z)}dz\right) \quad (5)$$

where α_{mol} (respectively α_{liq} and α_{ice}) is the molecular (respectively liquid and ice particles) extinction coefficient (m^{-1}), β_{mol} (respectively β_{liq} and β_{ice}) is the molecular (respectively liquid and ice particles) lidar backscatter coefficient ($m^{-1}\,sr^{-1}$), and η is the particulate multiple scattering coefficient taken equal to 0.7 following *Winker* [2003]. Sensitivity studies to this parameter have been conducted in *Chepfer et al.* [2007, 2008]. *Chepfer et al.* [2007, Figure 7] showed the lidar profiles simulated for different values of the multiple scattering coefficient. *Chepfer et al.* [2008, section 5.1, paragraph 17] demonstrated that changing the multiple scattering coefficient from 0.7 to 0.3 had a negligible impact (less than 1%) on the monthly mean total cloud fraction. Here we computed the low, middle, and high monthly mean cloud fractions for ice, liquid, undefined, and all clouds (Table 1). It confirms that the multiple scattering coefficient has a relatively small impact on the ice and liquid cloud fractions.

[25] For the phase diagnosis, we compute the liquid and ice backscatter (ATB_{liq} and ATB_{ice}), in complement to ATB and ATB_{mol}, i.e.,

$$\begin{aligned} ATB_{liq}(z) = &\left(\beta_{//,liq(z)} + \beta_{\perp,liq(z)} + \beta_{//,mol(z)} \right. \\ &\left. +\beta_{\perp,mol(z)}\right) \exp\left[-2\int_{Z}^{TOA}\left(\eta\alpha_{liq}(z) + \alpha_{mol}(z)\right)dz\right] \end{aligned} \quad (6)$$

$$\begin{aligned} ATB_{ice}(z) = &\left(\beta_{//,ice(z)} + \beta_{\perp,ice(z)} + \beta_{//,mol(z)} \right. \\ &\left. +\beta_{\perp,mol(z)}\right) \exp\left[-2\int_{Z}^{TOA}\left(\eta\alpha_{ice}(z) + \alpha_{mol}(z)\right)dz\right] \end{aligned} \quad (7)$$

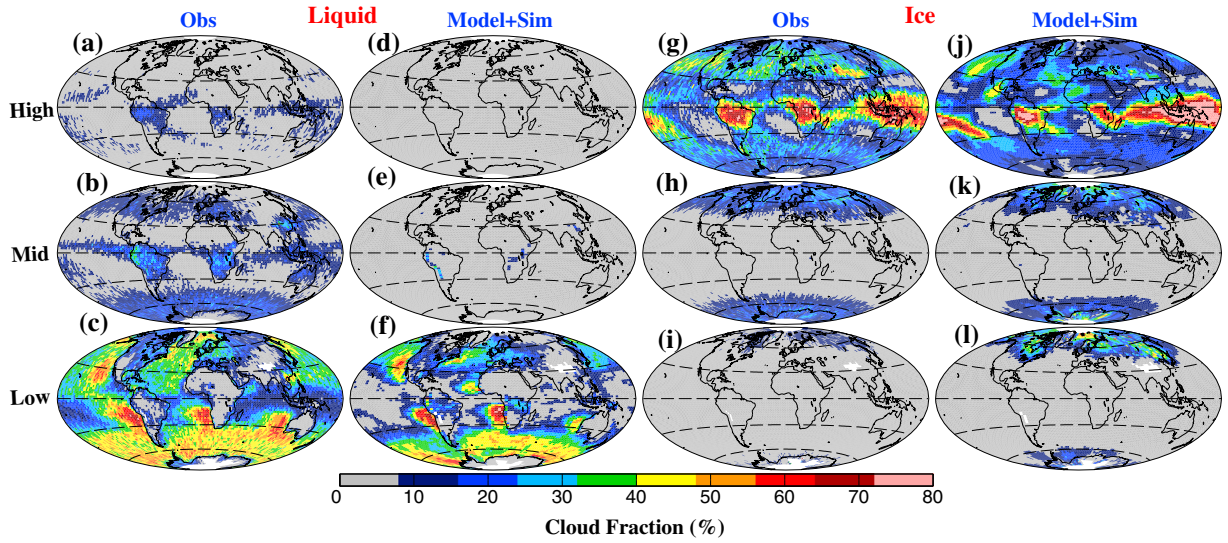

Figure 6. Ice and liquid cloud maps observed by CALIPSO-GOCCP and simulated by the "LMDZ GCM + COSP/lidar simulator" in JFM. Liquid cloud covers (a–c) observed and (d–f) simulated at high, middle, and low altitudes. Ice cloud covers (g–i) observed and (j–l) simulated at high, middle, and low altitudes.

[26] We then derive $ATB_{\perp,ice}$ ($ATB_{\perp,liq}$) from ATB_{ice} (ATB_{liq}) using a parameterization (Figure 5) deduced from the thinnest resolution of the observations (120 m). This allows taking into account the impact of multiple scattering on the ATB⊥ profile (for liquid and ice), as explained in section 2.3.2.

[27] We then compute $\beta_{\perp,ice}$ ($\beta_{\perp,liq}$) from $ATB_{\perp,ice}$ ($ATB_{\perp,liq}$) using the lidar equation in cross polarization, i.e.,

$$ATB_{\perp,ice(z)} = \left(\beta_{\perp,ice(z)} + \beta_{\perp,mol(z)}\right) \cdot \exp\left[-2\int_{Z}^{TOA}\left(\eta\alpha_{ice(z)} + \alpha_{mol(z)}\right)dz\right] \quad (8)$$

$$ATB_{\perp,liq(z)} = \left(\beta_{\perp,liq(z)} + \beta_{\perp,mol(z)}\right) \cdot \exp\left[-2\int_{Z}^{TOA}\left(\eta\alpha_{liq(z)} + \alpha_{mol(z)}\right)dz\right] \quad (9)$$

[28] Finally, the total ATB⊥ can be computed using $\beta_{\perp,ice}$ and $\beta_{\perp,liq}$, i.e.,

$$ATB_{\perp(z)} = \left(\beta_{\perp,liq(z)} + \beta_{\perp,ice(z)} + \beta_{\perp,mol(z)}\right) \cdot \exp\left[-2\int_{Z}^{TOA}\left(\eta\left(\alpha_{liq(z)} + \alpha_{ice(z)}\right) + \alpha_{mol(z)}\right)dz\right] \quad (10)$$

with

$$\beta_{\perp,mol(z)} = \left(\beta_{\perp,mol(z)} + \beta_{//,mol(z)}\right)/(1 + 1/\delta_{mol}) \quad (11)$$

where the molecular depolarization ratio is $\delta_{mol} = 0.0284$ [*Bodhaine et al.*, 1999].

[29] This computation provides profiles of ATB(z) and ATB⊥(z) at the subgrid scale over 40 vertical levels (480 m thick). Each level of the subgrid profile is either cloudy or not. Thus, water in non subgridded cloudy pixels can be liquid only, ice only, or a mix of both.

3.2. Statistics Over 3 Months

[30] The computation of ATB and ATB⊥ is applied to daily subgridded atmospheric profiles derived from LMDZ5B [*Hourdin et al.*, 2012] simulations, forced by observed sea surface temperatures. We computed 3 months of simulated subgrid daily CALIPSO-like profiles of total ATB and cross-polarized ATB⊥ to build phase diagrams for clouds with unambiguous phase (Figures 3d–3f), as we previously did with the observations (Figures 3a–3c). Cloudy pixels ($SR > 5$) below 3 km of altitude and warmer than 0°C are expected to be composed of liquid water. In a phase diagram (Figure 3e), most of these cloudy pixels are below the phase discrimination threshold (black curve), which classifies them as liquid water. A few pixels are above the threshold and correspond to very weak ATB (typically $<0.05\,km^{-1}\,sr^{-1}$) that can lead to false phase determination.

[31] Cloudy pixels above 8 km colder than −40°C are expected to be composed of ice. In a phase diagram (Figure 3f), these cloudy pixels are all well above the phase discrimination line (black curve), which correctly classifies them as ice. Initially, 2.1% of the ice clouds were below the black curve (and thus misclassified as liquid), which corresponded to clouds with values of ATB larger than $0.064\,km^{-1}\,sr^{-1}$ (ATB of the intersection point between the parameterized ice curve and the discrimination line). As those values of ATB are never encountered in the observations, they correspond to unrealistic optically thick clouds produced by the model. To avoid these phase misclassifications, when $ATB = ATB_{ice}$ and $ATB > 0.064\,km^{-1}\,sr^{-1}$, the values of ATB and ATB_{ice} are set to be $0.06\,km^{-1}\,sr^{-1}$ in the simulator. This impacts only the phase diagnostic in the lidar simulator and does not modify the cloud fraction that remains unchanged (not shown).

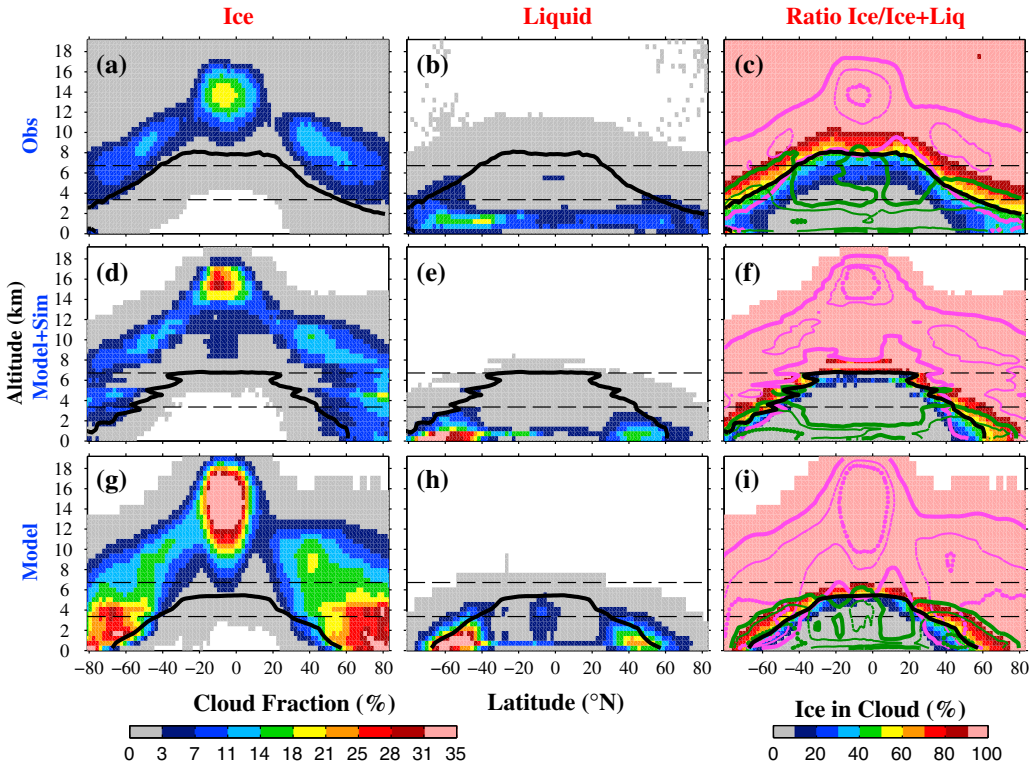

Figure 7. Cloud phase vertical distribution observed and simulated in JFM. (left column) Ice cloud fraction, (center) liquid cloud fraction, and (right) ice fraction with respect to the total condensate, (top row) for observations from CALIPSO-GOCCP, (middle row) for simulations by the "LMDZ GCM + COSP lidar simulator," and (bottom row) for simulations by LMDZ GCM alone, at a vertical resolution of $\Delta z = 480$ m. The black line corresponds to the equiprobability between liquid and ice (50%). The solid and dashed pink and green isolines show the ice (respectively 2%, 10%, and 18%) and liquid (respectively 2% and 6%) cloud fractions. The horizontal black dashed lines separate the low- and middle-level clouds (3.36 km) and the middle- and high-level clouds (6.72 km).

[32] Figure 3d shows the phase diagram, including all clouds regardless of their temperature (including also $-40°C < T < 0°C$): pixels spread on both sides of the phase discrimination line, indicating that some pixels contain both liquid and ice water in various proportions. Pixels containing mostly liquid and relatively little ice will show up below the threshold and will be classified as liquid, while those containing mostly ice and little liquid will be classified as ice. For consistency with the algorithm applied to the observations (section 2), the simulator also imposes that cloudy pixels with temperature $T > 0°C$ are classified as liquid, those with $T > -40°C$ are classified as ice, and those located below an optically thick cloud (SR > 30) are classified as "undefined."

4. Results

[33] We accumulated cloudy pixels collected over days to build global maps of low-altitude ($z < 3.36$ km), middle-altitude ($3.36 < z < 6.72$ km), and high-altitude ($6.72 < z < 19.2$ km) liquid and ice clouds, as well as global vertical distributions of ice and liquid clouds (at a resolution of 480 m). Detailed definitions of each variable can be found in Appendix A. Those daily variables are averaged over the JFM season.

4.1. Observed Liquid and Ice Clouds

[34] Figure 6 shows maps of liquid and ice clouds for low-, middle-, and high-altitude levels using five JFM seasons (2007–2011) of observations. As expected, high-altitude clouds (Figure 6, top row) are mostly composed of ice in the observations (Figure 6g). In middle-level clouds (Figure 6, second row), liquid water clouds occur (about 20%) in the warm middle latitudes and convective tropical regions [along the Intertropical Convergence Zone (ITCZ), Figure 6b], and ice clouds (typically 25%, Figure 6h) occur exclusively at high latitudes (poleward of 60°), where the middle troposphere is colder than at lower latitudes. Low-level clouds (Figure 6, bottom row) are almost exclusively composed of liquid (Figures 6c and 6i), except in polar regions where ice cloud cover reaches 20%.

[35] The zonal cloud fraction profile (Figure 7a) shows that ice clouds are observed only above 8 km in the tropics but appear at lower altitudes in middle- and high-latitude regions. Meanwhile, liquid clouds (Figure 7b) are mostly in the boundary layer, even if they reach the free troposphere at middle and high latitudes and in deep tropical convection. The partition between liquid and ice clouds (Figure 7c) shows equiprobability (50% ice and 50% liquid, represented by a solid black curve) is reached at lower altitudes in polar regions

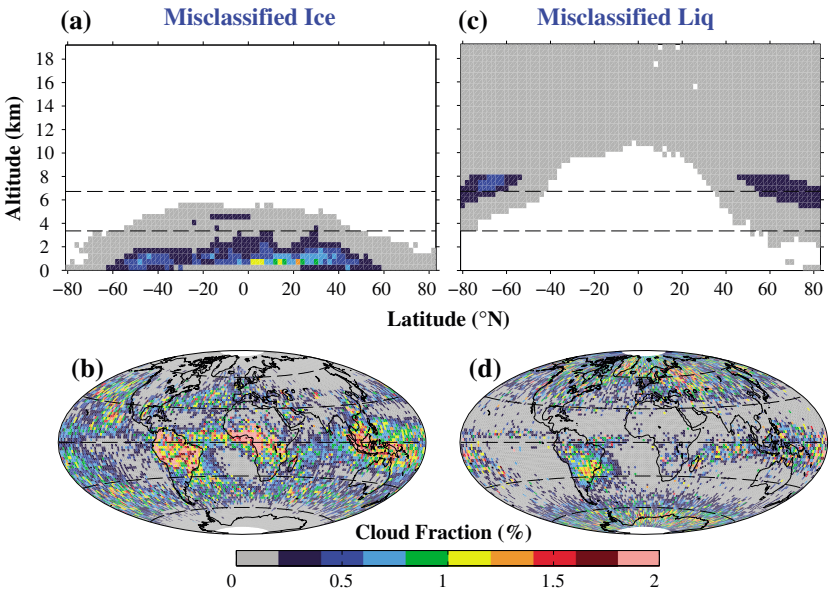

Figure 8. Misclassification in the observations. (a) Vertical distribution and (b) cloud maps of cloudy pixels misclassified as ice with $T > 0°C$. (c and d) Same as Figures 8a and 8b but for cloudy pixels misclassified as liquid with $T < -42°C$. The horizontal black dashed lines in Figures 8a and 8c separate the low- and middle-level clouds (3.36 km) and the middle- and high-level clouds (6.72 km).

compared to the tropics because of the temperature change with latitude at a given altitude. Areas of coexisting liquid and ice (blue to red color in Figure 7, right column) are significant at latitudes above 45° (middle latitudes and polar regions) but less in the tropics.

[36] We tested the sensitivity of these results to the position of the phase discrimination line in using the isolines 90% and 10% instead of 50% in Figure 4a. The results (not shown) are almost unchanged as only 1.3% of all the cloudy pixels are located between the isolines 10% and 90%. Moreover, our algorithm imposes that clouds with $T > 0°C$ are classified as liquid, and those with $T < -42°C$ are classified as ice. These temperature criteria are effectively used to classify the phase in less than 1% of the cloudy pixels. Figure 8 shows the regions where the temperature thresholds are used. Figures 8a and 8c indicate that the warm cloudy pixels ($T > 0°C$), initially misclassified as ice (based on ATB and $ATB_{\perp}$), are mostly located in the Saharan dust region, because the cross-polarized signal is produced by nonspherical dust. In these cases, the temperature criteria included in the algorithm allow avoiding misclassification. It is also useful in deep convection regions, where low liquid clouds located below high-altitude clouds would have been misclassified as ice if the temperature criteria had not been applied. For ice clouds (Figures 8b and 8d), the temperature threshold ($T < -42°C$) is mostly used in the South Atlantic anomaly region and over Greenland and Russia, likely because of the ground reflection.

[37] The transition temperature between liquid and ice varies between −20°C and −30°C depending on the latitude and the season (black line in Figures 13a and 13c). To characterize this transition, we used the temperature $T_{ice=liq}$ defined as the temperature where the ice and liquid cloud fractions are equiprobable (50%). In both seasons (not shown), deep convection (along the ITCZ) is associated with slightly warmer $T_{ice=liq}$ (−18°C) and subsidence tropical regions with colder $T_{ice=liq}$ (−33°C in June, July, August (JJA)). *Yoshida et al.* [2010] obtained warmer values of $T_{ice=liq}$ (−10°C) and compared with the results obtained using CALIPSO NASA Science Team Version 2 vertical feature mask $T_{ice=liq}$ (−20°C). The difference between NASA and *Yoshida et al.* [2010] results has been attributed to the contamination of oriented ice as water in the NASA product and to the different treatment of vertical layers (one phase for a whole layer in the Verticl Feature Mask (VFM) versus vertically resolved phase for *Yoshida et al.* [2010]). Moreover, differences between cloud detection in CALIPSO Version 3 Science Team product and CALIPSO-GOCCP have been documented [*Chepfer et al.*, 2013], showing significant differences between the cloud fractions, attributed to the difference in the resolution and the cloud detection threshold. As a consequence, for both cloud detection and phase discrimination, the vertical resolution used in the algorithm and the method used to discriminate ice and liquid discrimination have a significant impact on the results. Therefore, it is important to evaluate models against observations using the same definition for each cloud variables (resolution and thresholds).

4.2. Model Cloud Phase Diagnosed From the Lidar Simulator

[38] The daily cloud phase diagnostics are averaged over seasons to produce CALIPSO-like liquid and ice cloud maps (Figure 6) together with cloud ice (respectively liquid) vertical distribution (Figure 7d; respectively Figure 7e). The CALIPSO-like cloud ice (respectively liquid) vertical distribution (Figure 7d; respectively Figure 7e) is first compared with the cloud phase vertical distribution originally produced by LMDZ5B (Figure 7g; respectively Figure 7h). There are less clouds overall in the middle and lower troposphere when using the simulator. This is symptomatic of situations where high-level clouds mask low-level clouds, because the virtual lidar

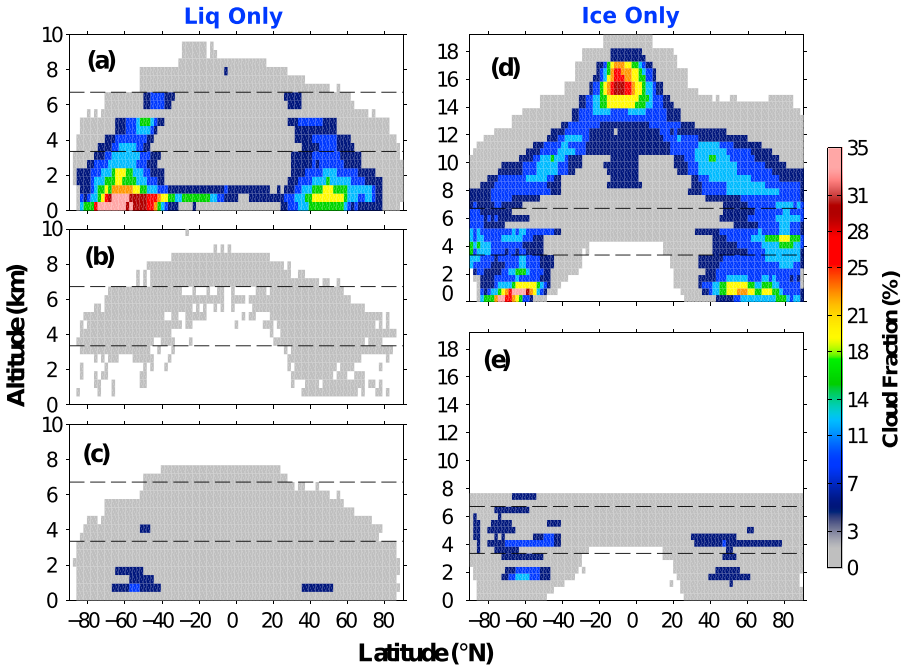

Figure 9. Misclassification in the simulations by the "LMDZ GCM + COSP lidar simulator." (left column) Vertical distribution of liquid clouds: (a) properly classified as liquid, (b) misclassified as ice, and (c) classified as undefined. (right column) Vertical distribution of ice clouds: (d) properly classified as ice and (e) classified as undefined. The horizontal black dashed lines separate the low- and middle-level clouds (3.36 km) and the middle- and high-level clouds (6.72 km).

laser cannot penetrate cloud with optical depths typically higher than 3. Less predictable, this masking effect affects more the ice clouds (Figure 7d compared to Figure 7g) than the liquid clouds (Figure 7e compared to Figure 7h). This is because a large majority of the clouds produced by LMDZ5B are composed of ice (Figure 7g compared to Figure 7h), and those clouds seem to have a significant optical depth.

[39] Figures 9a–9c quantify the liquid clouds that are misclassified as ice clouds or are undefined clouds due to the effect of the model+simulator. Figure 9a shows the CALIPSO-like liquid cloud fraction obtained when considering only liquid water (the ice water content is set to zero at the input of the simulator). The cloudy pixels misclassified as ice (Figure 9b) are mostly located in the upper troposphere and correspond to the pink boxes above the phase discrimination line in Figure 4b. They represent 0.28% of the cloudy pixels. The cloudy pixels (Figure 9c) that are classified as "undefined" because they are located below of clouds with SR > 30 are logically mainly located in the storm track region in the first kilometers above the surface. When considering only ice clouds (the liquid water content is set to zero at the input of the simulator), the resulting CALIPSO-like zonal ice cloud fraction profile is shown in Figure 9d. The cloudy pixels classified as "undefined" (Figure 9e) are also located in the storm track, just like the liquid clouds.

4.3. Evaluation of LMDZ5B Cloud Phase Against CALIPSO-GOCCP Observations

4.3.1. Main Features

[40] The model + simulator does not produce any liquid clouds above 3.2 km (Figures 6d and 6e), contrary to the observations (Figures 6a and 6b). Moreover, the model + simulator simulates too many ice high clouds along the ITCZ (Figure 6j) compared to the observations that show less ice high clouds (Figure 6g) and indicates the presence of liquid high clouds (Figure 6a). The main model + simulator defects are quantitatively summarized by zonal means (Figures 10a–10c): ice high clouds are underestimated at middle and high latitudes, and liquid low clouds are underestimated by about 30%, even more in the Southern Hemisphere middle latitudes (see also Figure 6). Independently of the cloud cover, the model + simulator fails to reproduce the ice and liquid partition within clouds (Figure 10d) in 30%–40% of polar low clouds, in up to 30% of tropical high clouds, and in 40% of middle-level clouds at middle and low latitudes. The vertical distributions (Figure 7) clearly indicate that the model produces ice instead of liquid water at low altitudes in polar regions. Moreover, the model + simulator fails to reproduce correctly the coexistence of ice and liquid clouds. In the observations (Figure 7c), ice and liquid clouds coexist over a 4 km vertical range at all latitudes. In the model (Figure 7f), liquid and ice clouds almost never coexist: no liquid clouds are found where ice clouds occur (and vice versa).

4.3.2. Role of Temperature

[41] Observed ice clouds are dominant (Figure 11a) within a wide range of temperatures between −21°C and −90°C, with a maximum cloud fraction around −43.5°C. As expected from theory and from the previous sections, liquid and ice clouds coexist between 0°C and −40°C. Liquid clouds occur at temperatures as cold as −40°C, in agreement with in situ measurements of liquid droplets at −40.7°C [*Heymsfield and Miloshevich*, 1993] and ground-based lidar retrievals [*Noel et al.*, 2006]. By contrast,

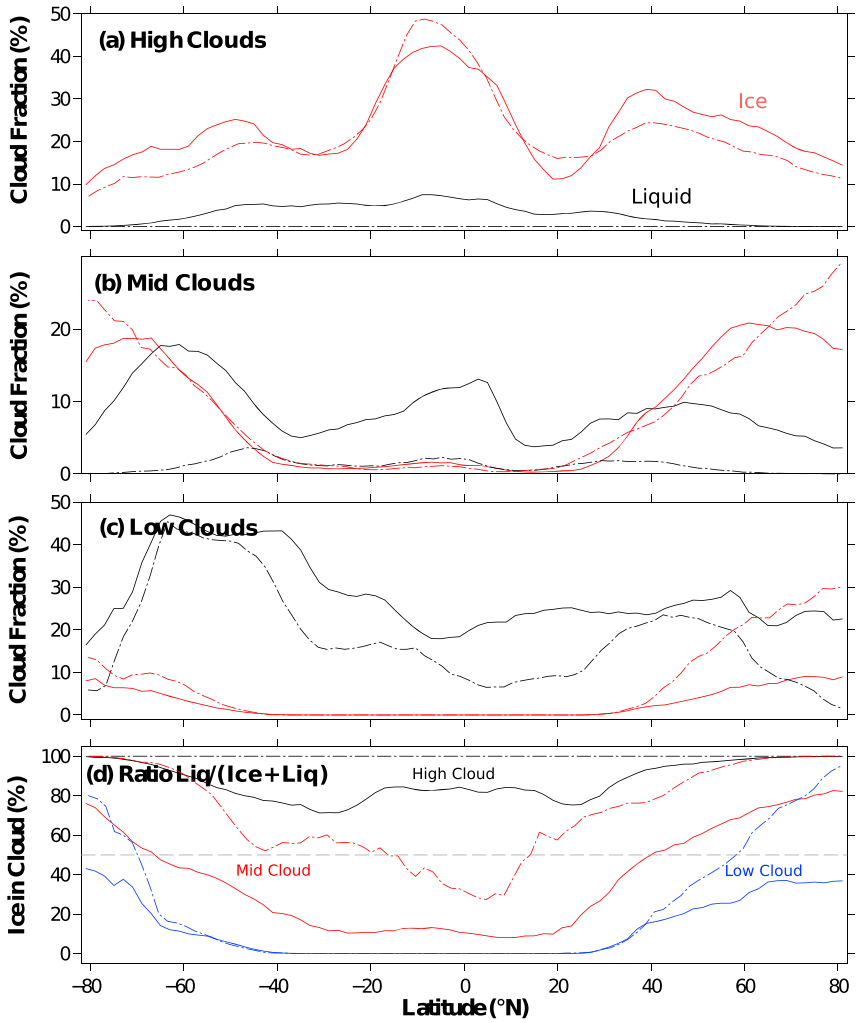

Figure 10. Zonal means of low, middle, and high cloud covers, (solid lines) as observed by CALIPSO-GOCCP and (dash-dotted lines) as simulated by the "LMDZ GCM + COSP lidar simulator" in JFM. (a) High, (b) middle, and (c) low cloud covers are represented by black lines for liquid and red lines for ice. (d) Ice fraction with respect to the total condensate is represented by black lines for high clouds, red lines for middle clouds, and blue lines for low clouds.

the "model + simulator" (dash-dotted lines) does not produce liquid clouds colder than −20°C. Moreover, most liquid clouds are observed between −21°C and 21°C with two maxima at −10.5°C and 16.5°C. While the "model + simulator" correctly produces a bimodal liquid cloud distribution consistent with observations, its maximum within the negative temperatures is too warm (−7.5°C). Nevertheless, in all regions (Figure 11b), the transition between liquid- and ice-dominated clouds is too warm by about 9°C in the "model + simulator" (colored dashed lines), and the temperature range in which liquid and ice coexist is way too narrow (~10°C) compared to the observations (~35°C, colored solid + circle line). This is a direct consequence of the cloud phase parameterization in LMDZ5B [*Hourdin et al.*, 2012] that imposes the transition between ice and liquid around −7.5°C. The relationship used inside the LMDZ's parameterization is reported in Figure 11b (black dash-dotted line) together with the "LMDZ GCM alone" cloud phase transition (solid black line) obtained from outputs of the model. When the attenuation of the lidar signal is taken into account (black dashed line in Figure 11b), the transition between liquid and ice is shifted to a colder value (−12°C instead of −7.5°C) but still remains too warm compared to the observations (−20°C, black solid + circle line). Therefore, the shift from −12°C to −7.5°C (black solid line versus black dashed line) is due to the peculiarities of the lidar instrument (e.g., cloud detection, lidar attenuation, and multiple scattering). In addition to this warm bias, the model also produces a significant amount of very cold ice clouds ($T < -60$°C) stuck to the tropopause (Figure 12), especially in middle and high latitudes, that do not exist in the observations.

5. Conclusion and Perspectives

[42] In order to evaluate how climate models describe the partition between liquid and ice clouds, we built a liquid and ice cloud climatology using CALIOP Level 1 version 3 observations and a cloud phase diagnosis within the COSP

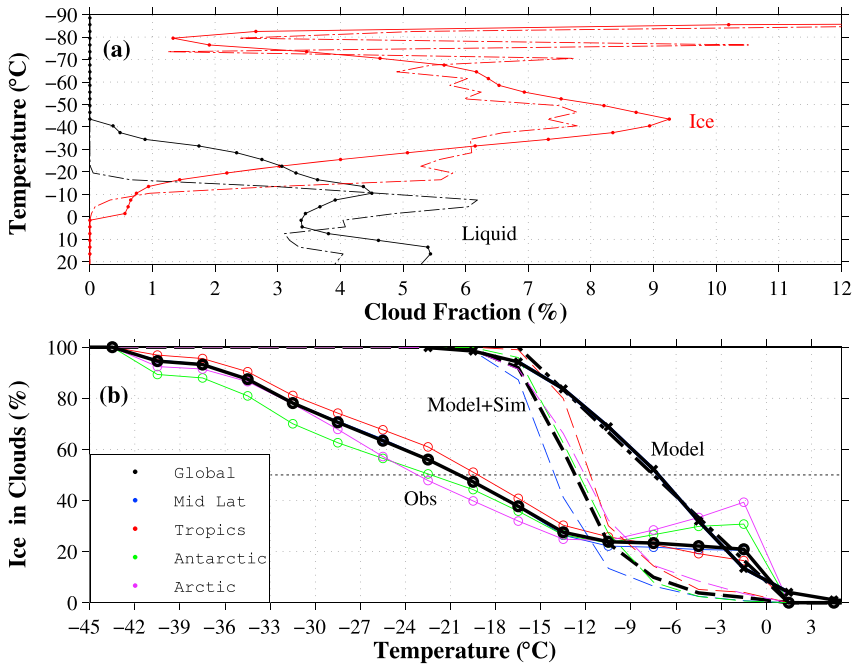

Figure 11. Temperature profiles in liquid and ice clouds. (a) Temperature profiles of (black) liquid and (red) ice clouds in JFM, (solid lines) as observed by CALIPSO-GOCCP and (dash-dotted lines) as simulated by the "LMDZ GCM + COSP lidar simulator." Note that the high values of cloud fraction at temperature colder than −80°C correspond to very few cloudy events (0.8% of ice clouds). (b) Ice fraction with respect to the total condensate, (solid + circle lines) as observed by CALIPSO-GOCCP and (dashed lines) as simulated by the "LMDZ GCM + COSP lidar simulator" for different regions. The modeled temperature in each subgrid is vertically averaged over 480 m to characterize the temperature of each cloudy pixel. The black solid line corresponds to ice fraction with respect to the total condensate as simulated by LMDZ GCM vertically averaged over the 480 m GOCCP grid. The dash-dotted black line corresponds to the relationship used to parameterize the phase transition in LMDZ GCM.

lidar simulator. Definitions of ice and liquid clouds within the observational data set and the simulator are fully consistent, so that the differences between observations and outputs from the ensemble "model + simulator" can be used to evaluate the cloud thermodynamic phase in the model.

[43] The liquid and ice cloud climatology is new in the GCM-oriented CALIPSO Cloud Product (CALIPSO-GOCCP). It was built using lidar profiles of total attenuated backscatter (ATB) and cross-polarized attenuated backscatter (ATB⊥) included in the CALIOP Level 1 data set (version 3). Each level of altitude (480 m thick) of a single lidar profile (every 330 m) is declared cloudy when the scattering ratio (SR) is higher than 5. The values of cross-polarized and total attenuated backscattered signals were used to determine liquid or ice cloud particle phase. The sensitivity of the ice/liquid discrimination was discussed. We then documented ice and

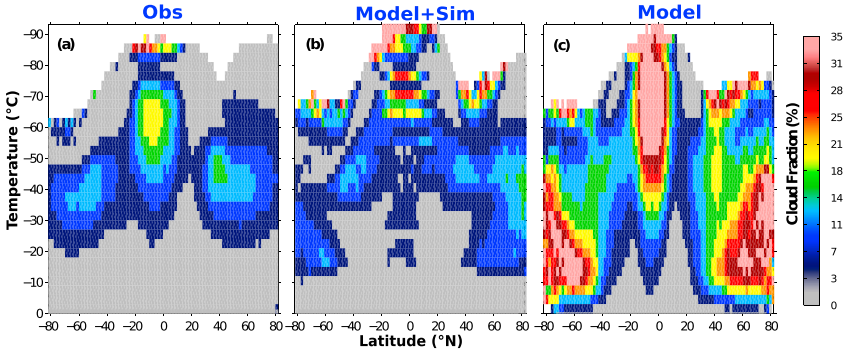

Figure 12. Cloud temperature distribution. Ice cloud fraction in JFM (a) as observed by CALIPSO-GOCCP in JFM, (b) as simulated by the "LMDZ GCM + COSP lidar simulator," and (c) as simulated by LMDZ GCM alone.

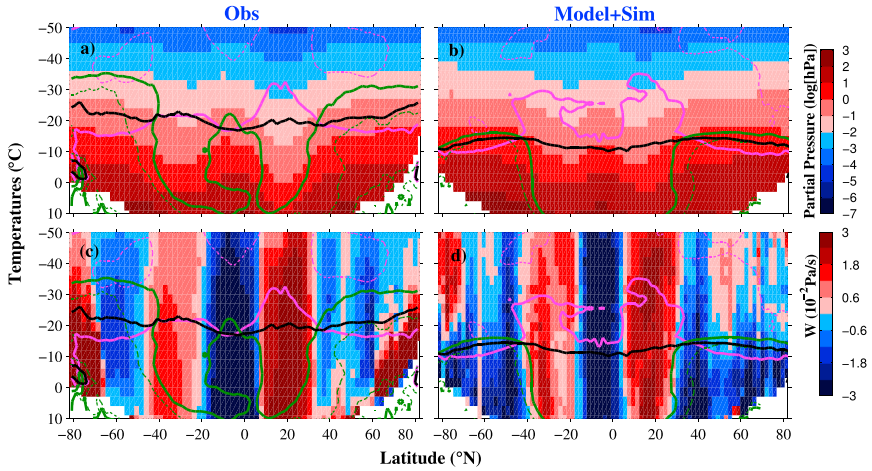

Figure 13. Cloud phase as a function of the atmospheric humidity and vertical wind speed. (a) Logarithm of partial pressure of water vapour from the European Centre for Medium-Range Weather Forecast Reanalysis (ERA) interim in JFM. (c) Vertical wind speed from ERA interim in JFM (10^{-2} Pa/s). (b and d) Same as Figures 13a and 13c but simulated by the "LMDZ GCM + COSP lidar simulator" and using the LMDZ thermodynamical fields. The black line corresponds to the equiprobability between liquid and ice. The solid and dashed pink and green isolines show the ice (respectively 2%, 10%, and 18%) and liquid (respectively 2% and 6%) cloud fractions.

liquid clouds observed along a single CALIPSO orbit. We built global maps of liquid and ice clouds in low-, middle-, and high-altitude levels and zonal vertical distributions (40 levels) of liquid and ice clouds, accumulating five JFM seasons of observations (2007–2011).

[44] We analyzed the link between the cloud phase observed by CALIPSO-GOCCP and the cloud temperature given independently by ancillary data. Liquid water still exists at temperatures as cold as −35°C in tropical regions. The ice-liquid equiprobability (coexistence of 50% of ice with 50% of liquid) typically occurs at −21°C but varies with the humidity in the upper troposphere in the observations (±5 K). It is colder in the drier conditions of tropical subsidence and above land in polar regions.

[45] A cloud phase diagnosis has been developed in the COSP lidar simulator. We first computed, from model outputs, ATB and ATB⊥ lidar profiles in each subgrid, then classified each cloudy pixel within a profile as a liquid or ice cloud using the phase discrimination line ("the black curve") on ATB and ATB⊥ as in the observations, and finally built statistics by accumulating one season of simulations. We built maps of liquid and ice clouds and vertical distributions of liquid and ice clouds from the ensemble "climate model + simulator," similar to the ones that were obtained from a lidar flying over the atmosphere predicted by the model. This method allows taking into account the vertical and horizontal resolutions, the masking of low clouds by high clouds, the effects of multiple scattering on polarization measurements by the virtual lidar, the attenuation of the lidar signal, etc.

[46] We compared the liquid and ice cloud vertical distributions simulated by the model with and without the simulator. Results show that optically thick high clouds mask lower clouds in some regions (mostly storm tracks), as the lidar cannot penetrate through clouds with optical depths higher than 3. A sensitivity study has shown that the results are poorly sensitive to the parameters used in the simulator (the multiple scattering factor and the position of the phase discrimination line). Moreover, very few misclassified phase clouds (less than 0.3%) are introduced by the use of the lidar simulator.

[47] The comparison between observations and simulations shows that the LMDZ5B model significantly underestimates the amount of liquid water in clouds (no liquid clouds above 3 km) and produces ice instead of liquid clouds everywhere, particularly over polar regions at low and middle levels and in the upper troposphere at middle latitudes and along the ITCZ. The transition from liquid to ice typically occurs around −21°C in the observations, whereas it appears at −12°C in the model + simulator and at −7.5°C in the model parameterization The model does not reproduce any coexistence of liquid and ice, even though this occurs frequently in the observations over a wide range of temperature (0°C to −40°C). Moreover, the transition between ice and liquid water in the model is independent of the atmospheric humidity, in contrast to observations where the amount of liquid and ice clouds at a given temperature depends on humidity. Even if the lidar simulator shifts the model cloud phase parameterization to colder temperature because of the lidar instrument peculiarities, the cloud phase parameterization remains too warm compared to observations. It clearly appears that the cloud phase parameterization currently used in LMDZ is not appropriate.

[48] Future work will include (1) a change in LMDZ cloud phase parameterization based on these results; (2) a comparison of our phase partitioning algorithm with other satellite climatologies as well as with ground-based and in situ observations; and (3) a study of the link between the cloud thermodynamic phase, temperature, humidity, and wind. In the strong subsidence regions (40°S–20°S and 10°N–30°N, red area in Figure 13c), where the atmosphere is drier than that at other latitudes (Figure 13a), there is no

overlap between liquid and ice clouds (green and pink isocontours). On the other hand, at the equator and at middle and high latitudes, where the atmosphere is wetter, liquid and ice clouds coexist. In these regions, it seems that the liquid and ice equiprobability temperature is correlated to the partial pressure of the water vapor: they are increasing together moving poleward. The model does not replicate the observations at middle and high latitudes: "$T_{ice=liq}$" decreases, whereas the partial pressure of water vapor is constant. This could be due to the modeled vertical wind that is different from the observed one in polar regions. Additional work, based on the same observations at a higher spatiotemporal resolution, will be pursued to study the link between the cloud phase, temperature, humidity, and wind in both the model and the observations.

[49] The CALIPSO-GOCCP cloud phase climatology is available on the CFMIP-OBS website (http://climserv.ipsl.polytechnique.fr/cfmip-obs/Calipso_goccp.html).

[50] The new version of the lidar simulator, including the cloud phase diagnosis, will be included in the next release of COSP (http://cfmip.metoffice.com/COSP.html) for evaluating the ice and liquid cloud distributions in other climate models.

Appendix A: Definition of the Global-Scale Statistical Diagnostic

A1. Maps of Liquid and Ice Clouds

[51] We split the atmosphere in three altitude layers [*Chepfer et al*, 2010]: low ($z < 3.36$ km), middle ($3.36 < z$ 6.72 km), and high ($6.72 < z < 19.2$ km). For each layer, we built maps of liquid (Figures 6a–6f), ice (Figures 6g–6l), and undefined clouds. As an example, the map of liquid low clouds is built as follows: (1) for each lidar profile, the low layer ($z < 3.36$ km) is flagged "cloudy" if the profile contains at least one cloudy pixel (identified in section 4.1); (2) for each lidar profile, the low layer is flagged "liquid" if it contains at least one "liquid" cloudy pixel; (3) we computed the total number of low cloudy layers (Ncloud) and the number of liquid low cloudy layers ($Ncloud_{liq}$) accumulated during a day within a latitude-longitude grid box; and (4) we computed the liquid low cloud fraction ($CF_{low,liq}$) in each latitude-longitude box for each day, i.e.,

$$CF_{low,liq} = Ncloud_{liq}/Ncloud \times CF_{low} \quad (12)$$

where CF_{low} is computed by dividing, for each longitude-latitude grid box, the number of cloudy profiles encountered for 1 day by the total number of instantaneous SR profiles (not fully attenuated) measured during that day [*Chepfer et al*., 2010].

[52] To complete these maps of liquid low cloud fraction, we similarly computed maps of ice low cloud fraction ($CF_{low,ice}$) and undefined low cloud fraction ($CF_{low,undef}$). These low cloud fractions are linked by the following relationship:

$$CF_{low} = CF_{low,liq} + CF_{low,ice} + CF_{low,undef} \quad (13)$$

[53] To study directly the water phase partition within the clouds, we defined the cloud phase ratio (e.g., CPR_{low} for low clouds), which documents the relative part of ice and liquid within clouds independently of the cloud cover. Maps of the cloud phase ratio for each day in each layer (low, middle, or high) describe the ratio between the number of ice layers and the number of ice and liquid layers in each latitude-longitude box for each day. A cloud phase ratio of 100 means the layer (low, middle, or high) contains only ice clouds, whereas a cloud phase ratio of 0 corresponds to a layer that contains only liquid clouds.

A2. Vertical Distribution of Liquid and Ice Clouds

[54] In addition to cloud phase maps, and to obtain a more detailed view of the vertical distribution of cloud phase, we define the 3-D cloud phase fraction.

[55] The liquid (respectively ice and undefined) 3-D cloud fraction $CF3D_{liq}$ (respectively $CF3D_{ice}$ and $CF3D_{undef}$) is computed for each profile vertical level (480 m) by dividing, for each latitude longitude grid box, the number of liquid (respectively ice and undefined) cloudy pixels by the total number of pixels measured. Fully attenuated pixels ($0 < SR < 0.01$) are not taken into account [*Chepfer et al*., 2010].

[56] In each latitude-longitude-altitude grid box, the total 3-D cloud fraction (called "CF3D" in CALIPSO-GOCCP) [*Chepfer et al*., 2010] is equal to the sum of the three-phase 3-D cloud fractions, i.e.,

$$CF3D = CF3D_{liq} + CF3D_{ice} + CF3D_{undef} \quad (14)$$

[57] As discussed previously, we also computed a variable ($CF3DP_{ice/liq}$) independent of the 3-D cloud fraction (CF3D) to study the partition between ice and liquid clouds. $CF3DP_{ice/liq}$ is the ratio between the number of ice cloud pixels and the sum of ice and liquid cloud pixels at each level of altitude. $CF3DP_{ice/liq} = 100$ when a given level contains only ice clouds and 0 when it contains only liquid water clouds.

[58] **Acknowledgments.** Thanks are due to NASA and CNES for CALIOP Level 1 data. We would like to thank Vincent Noel for internal review and the CLIMSERV/CGTD for access Level 1 data and CLIMSERV/ICARE for computing facility.

[59] The authors would like to thank the three anonymous reviewers for their help in improving the manuscript.

References

Barnes, W. L., T. S. Pagano, and V. V. Salomonson (1998), Prelaunch characteristics of the Moderate Resolution Imaging Spectroradiometer (MODIS) on EOS-AM1, *IEEE Trans. Geosci. Remote Sens.*, *36*, 1088–1100, doi:10.1109/36.700993.

Bey, I., D. J. Jacob, R. M. Yantosca, J. A. Logan, B. D. Field, A. M. Fiore, Q. Li, H. Y. Liu, L. J. Mickley, and M. G. Schultz (2001), Global modeling of tropospheric chemistry with assimilated meteorology: Model description and evaluation, *J. Geophys. Res.*, *106*(D19), 23,073–23,095, doi:10.1029/2001JD000807.

Bodas-Salcedo, A., M. J. Webb, M. E. Brooks, M. A. Ringer, K. D. William, S. F. Milton, and D. R. Wilson (2008), Evaluating cloud systems in the Met Office global forecast model using simulated CloudSat radar reflectivities, *J. Geophys. Res.*, *113*, D00A13, doi:10.1029/2007JD009620.

Bodas-Salcedo, A, et al. (2011), COSP: Satellite simulation software for model assessment. *Bull. Am. Meteorol. Soc.*, *92*, 1023–1043, doi:10.1175/2011BAMS2856.

Bodhaine, B. A., N. B. Wood, E. G. Dutton, and J. R. Slusser (1999), On Rayleigh optical depth calculations. *J. Atmos. Oceanic Technol.*, *16*, 1854–1861, doi:10.1175/1520-0426(1999)016<1854:ORODC>2.0.CO;2.

Cesana, G., and H. Chepfer (2012), How well do climate models simulate cloud vertical structure?—A comparison between CALIPSO-GOCCP satellite observations and CMIP5 models, *Geophys. Res. Lett.*, *39*, L20803, doi:10.1029/2012GL053153.

Cesana, G., J. E. Kay, H. Chepfer, J. English, and G. de Boer (2012), Ubiquitous low-level liquid-containing Arctic clouds: New observations and climate model constraints from CALIPSO-GOCCP, *Geophys. Res. Lett.*, *39*, L20804, doi:10.1029/2012GL053385.

Cheng, A., K.-M. Xu, Y. Hu, and S. Kato (2012), Impact of a cloud thermodynamic phase parameterization based on CALIPSO observations on climate simulation, *J. Geophys. Res.*, *117*, D09103, doi:10.1029/2011JD017263.

Chepfer H., M. Chiriaco, R. Vautard, and J. Spinhirne (2007), Evaluation of the ability of MM5 meso-scale model to reproduce optically thin clouds over Europe in fall using ICE/SAT lidar space-born observations, *Mon. Weather Rev.*, *135*(7), 2737–2753, doi:10.1175/MWR3413.1.

Chepfer, H., S. Bony, D. M. Winker, M. Chiriaco, J.-L. Dufresne, and G. Seze (2008), Use of CALIPSO lidar observations to evaluate the cloudiness simulated by a climate model, *Geophys. Res. Lett.*, *35*, L15704, doi:10.1029/2008GL034207.

Chepfer, H., S. Bony, D. Winker, G. Cesana, J. L. Dufresne, P. Minnis, C. J. Stubenrauch, and S. Zeng (2010), The GCM oriented CALIPSO Cloud Product (CALIPSO-GOCCP), *J. Geophys. Res.*, *115*, D00H16, doi:10.1029/2009JD012251.

Chepfer, H., G. Cesana, D. Winker, B. Getzewich, and M. Vaughan (2013), Comparison of two different cloud climatologies derived from CALIOP Level 1 observations: The CALIPSO-ST and the CALIPSO-GOCCP, *J. Atmos. Oceanic Technol.*, *30*, 725–744, doi:10.1175/JTECH-D-12-00057.1.

Deschamps, P. Y., F. M. Bréon, M. Leroy, A. Podaire, A. Bricaud, J. C. Buriez, and G. Sèze (1994), The POLDER mission: Instrument characteristics and scientific objectives, *IEEE Trans. Geosci. Remote Sens.*, *32*, 598–615, doi:10.1109/36.297978

Doutriaux-Boucher, M., and J. Quaas (2004), Evaluation of cloud thermodynamic phase parametrizations in the LMDZ GCM by using POLDER satellite data, *Geophys. Res. Lett.*, *31*, L06126, doi:10.1029/2003GL019095.

Goloub, P., M. Herman, H. Chepfer, J. Riedi, G. Brogniez, P. Couvert, and G. Séze (2000), Cloud thermodynamical phase classification from the POLDER spaceborne instrument, *J. Geophys. Res.*, *105*(D11), 14,747–14,759, doi:10.1029/1999JD901183.

Heymsfield, A. J., and L. M. Miloshevich (1993), Homogeneous ice nucleation and supercooled liquid water in orographic wave clouds, *J. Atmos. Sci.*, *50*, 2335–2353, doi:10.1175/1520-0469(1993)050<2335:HINASL>2.0.CO;2.

Hourdin, F., et al. (2012), LMDZ5B: The atmospheric component of the IPSL climate model with revisited parameterizations for clouds and convection, Clim. Dyn., doi:10.1007/s00382-012-1343-y, in press.

Hu, Y. (2007), Depolarization ratio-effective lidar ratio relation: Theoretical basis for space lidar cloud phase discrimination, *Geophys. Res. Lett.*, *34*, L11812, doi:10.1029/2007GL029584.

Hu, Y., D. Winker, P. Yang, B. A. Baum, L. Poole, and L. Vann (2001), Identification of cloud phase from PICASSO-CENA lidar depolarization: A multiple scattering sensitivity study, *J. Quant. Spectrosc. Radiat. Transfer*, *70*, 569–579, doi:10.1016/S0022-4073(01)00030-9.

Hu, Y., et al. (2009), CALIPSO/CALIOP cloud phase discrimination algorithm, *J. Atmos. Oceanic Technol.*, *26*(11), 2293–2309, doi:10.1175/2009JTECHA1280.1.

Hu, Y., S. Rodier, K. Xu, W. Sun, J. Huang, B. Lin, P. Zhai, and D. Josset (2010), Occurrence, liquid water content, and fraction of supercooled water clouds from combined CALIOP/IIR/MODIS measurements, *J. Geophys. Res.*, *115*, D00H34, doi:10.1029/2009JD012384.

Kiehl, J. T., and K. E. Trenberth (1997) Earth's annual global mean energy budget, *Bull. Am. Meteorol. Soc.*, *78*, 197–208.

Klein, S. A., and C. Jakob (1999), Validation and sensitivities of frontal clouds simulated by the ECMWF model, *Mon. Weather Rev.*, *127*(10), 2514–253, doi:10.1175/1520-0493(1999)127<2514:VASOFC>2.0.CO;2.

Marchand, R., and T. Ackerman (2010), An analysis of cloud cover in multiscale modeling framework global climate model simulations using 4 and 1 km horizontal grids, *J. Geophys. Res.*, *115*, D16207, doi:10.1029/2009JD013423.

Marchand, R., J. Haynes, G. G. Mace, T. Ackerman, and G. Stephens (2009), A comparison of simulated cloud radar output from the multiscale modeling framework global climate model with CloudSat cloud radar observations, *J. Geophys. Res.*, *114*, D00A20, doi:10.1029/2008JD009790.

Mishchenko, M. I., and L. D. Travis (1997), Satellite retrieval of aerosol properties over the ocean using polarization as well as intensity of reflected sunlight, *J. Geophys. Res.*, *102*, 16,989–17,013, doi:10.1029/96JD02425.

Noel, V., and H. Chepfer (2010), A global view of horizontally oriented crystals in clouds from CALIPSO, *J. Geophys. Res.*, 115, D00H23, doi:10.1029/2009JD012365.

Noel, V., H. Chepfer, M. Haeffelin, and Y. Morille (2006), Classification of ice crystal shapes in midlatitude ice clouds from three years of lidar observations over the SIRTA observatory, *J. Atmos. Sci.*, *63*, 2978–2991, doi:10.1175/JAS3767.1.

Pal, S. R., and A. l. Carswell (1985), Polarization anisotropy in lidar multiple scattering from atmospheric clouds, *Appl. Opt.*, *24*(21), 3464–3471, doi:10.1364/AO.24.003464.

Pincus, R., S. Platnick, S. A. Ackerman, R. S. Hemler, and R. J. P. Hofmann (2012), Reconciling simulated and observed views of clouds: MODIS, ISCCP, and the limits of instrument simulators. *J. Clim.*, 25, 4699–4720, doi:10.1175/JCLI-D-11-00267.1.

Platnick, S., M. D. King, S.A. Ackerman, W.P. Menzel, B.A. Baum, J. C. Riedi, and R.A. Frey (2003), The MODIS cloud products: Algorithms and examples from Terra, *IEEE Trans. Geosci. Remote Sens.*, *41* (2), 459–473, doi:10.1109/TGRS.2002.808301.

Platt, C. M. R. (1981), Remote sounding of high clouds. III: Monte Carlo calculations of multiple-scattered lidar returns, *J. Atmos. Sci.*, *38*, 156–167, doi:10.1175/1520-0469(1981)038<0156:RSOHCI>2.0.CO;2.

Rossow, W. B., and R. A. Schiffer (1999), Advances in understanding clouds from ISCCP, *Bull. Am. Meteorol. Soc.*, *80*, 2261–2288, doi:10.1175/1520-0477(1999)080<2261:AIUCFI>2.0.CO;2.

Sassen, K., and R. L. Petrilla (1986), Lidar depolarization from multiple scattering in marine stratus clouds, *Appl. Opt.*, *25*(9), 1450–1459, doi:10.1364/AO.25.001450.

Taylor, K. E., R. J. Stouffer, G. A. Meehl (2012), An overview of CMIP5 and the experiment design, *Bull. Am. Meteorol. Soc.*, *93*, 485–498, doi:10.1175/BAMS-D-11-00094.1.

Van de Hulst, H. C. (1957), *Light Scattering by Small Particles*, Dover, New York.

Webb, M., C. Senior, S. Bony, and J. J. Morcrette (2001), Combining ERBE and ISCCP data to assess clouds in the Hadley Centre, ECMWF and LMD atmospheric climate models, *Clim. Dyn.*, *17*, 905–922, doi:10.1007/s003820100157.

Winker, D. M. (2003), Accounting for multiple scattering in retrievals from space lidar, *SPIE*, 5059, doi:10.1117/12.512352.

Winker, D. M., M. A. Vaughan, A. H. Omar, Y. Hu, K. A. Powell, Z. Liu, W. H. Hunt, and S. A. Young (2009), Overview of the CALIPSO mission and CALIOP data processing algorithms, *J. Atmos. Oceanic Technol.*, *26*, 2310–2323, doi:10.1175/2009JTECHA1281.1.

Yokohata, T., S. Emori, T. Nozawa, Y. Tsushima, T. Ogura, and M. Kimoto (2005), Climate response to volcanic forcing: Validation of climate sensitivity of a coupled atmosphere-ocean general circulation model, *Geophys. Res. Lett.*, *32*, L21710, doi:10.1029/2005GL023542.

Yoshida, R., H. Okamoto, Y. Hagihara, and H. Ishimoto (2010), Global analysis of cloud phase and ice crystal orientation from Cloud-Aerosol Lidar and Infrared Pathfinder Satellite Observation (CALIPSO) data using attenuated backscattering and depolarization ratio, *J. Geophys. Res.*, *115*, D00H32, doi:10.1029/2009JD012334.

Zhang, M. H., et al. (2005), Comparing clouds and their seasonal variations in 10 atmospheric general circulation models with satellite measurements, *J. Geophys. Res.*, *110* (D15), D15S02, doi:10.1029/2004JD005021.

Erratum

The URL to the CALIPSO-GOCCP cloud phase climatology, found in Conclusions and Perspectives, contained a hyphen that was incorrectly typeset; the link did not function as published. The correction has been made to the online version of this article, but not the PDF, and the online version may be considered the authoritative version of record.